Effects of symmetry-breaking mechanisms on the flow field around magnetic-responsive material appendages that mimic swimming strokes

Mohammad Mohaghar ®,[1,*] Angelica A. Connor,[1,2] Shuai Wu,[3]
Ruike Renee Zhao,[3] and Donald R. Webster ®[1]

[1]*School of Civil and Environmental Engineering, Georgia Institute of Technology, 790 Atlantic Drive, Atlanta, Georgia 30332, USA*
[2]*George W. Woodruff School of Mechanical Engineering, Georgia Institute of Technology, Atlanta, Georgia 30332, USA*
[3]*Department of Mechanical Engineering, Stanford University, Stanford, California 94305, USA*

The flow field around bioinspired magnetic-responsive soft materials that mimic the symmetry-breaking mechanisms in swimming animals, such as pteropods and manta rays, is studied using the tomographic particle image velocimetry (tomo-PIV) technique. Magnetic-responsive material appendages are actuated by an oscillating external magnetic field. The fluid flow induced by two types of actuation is quantified. First, a single actuation mode involves alternating upward and downward bending motions. Second, an asymmetric multimodal actuation encompasses upward folding and downward bending motions by locating an asymmetric joint at the midpoint of the appendage. The formed vorticity field, vortex structure, and viscous energy dissipation rate in the surrounding fluid are observed to be weaker for the multimodal actuation case. The multimodal appendage moves with reduced flow resistance, leading to faster appendage velocity during the downward power stroke. Furthermore, the study examines the effect of an asymmetric magnetic field cycle on the flow field by extending the time interval of the applied positive voltage (upstroke motion) compared to the duration of the negative applied voltage (downstroke motion). The asymmetric cycle and extended stopping period provide time for greater dissipation of the formed vorticity field. Thus, the peak values of vorticity and viscous dissipation rate decrease to smaller magnitudes compared to the symmetric cycle case. These findings demonstrate that the utilization of symmetry-breaking morphology and an asymmetric cycle enhances stroke performance, offering promising avenues for achieving greater effectiveness in underwater propulsion.

I. INTRODUCTION

The shape and movement of wings or fins significantly impact the speed, direction, and performance of animal propulsion [1–5]. Rigid propulsor models are often used in the study of animal propulsion due to their simplicity and relative ease of mathematical analysis [6,7]. This simplification can make it easier to understand the basic mechanics of propulsion; however, rigid propulsors have limitations in accurately representing the complex, flexible structures used for propulsion in real animals [8,9]. The elastic deformation (or bending) and rigid body rotation (or folding) of propulsor structures are essential factors in generating hydrodynamic forces that propel the animal. These factors affect the production of lift and drag forces, which alter swimming speed and direction

---

*mohaghar@gatech.edu

[10–15]. Further, the angle at which a wing is bent or folded, called the wing flexion angle, affects the hydrodynamic wake generated by the propulsor, which alters swimming performance. Lucas *et al.* [9] found remarkable consistency in the propulsor flexion angle, between 20º to 40º, for a wide range of swimming and flying animals, from the winglike parapodia of pteropod molluscs to the fins of fish, such as manta rays. It is clear that the flexibility and curvature of the wings, as well as the stopping time between wing-flapping cycles (also known as the interstroke interval), play a critical role in determining the performance of the animal's swimming stroke [16–22].

To study the mechanics of animal propulsion and develop technologies based on these principles, stimuli-responsive soft materials represent an exciting area of research in biophysics and bioinspired engineering [23–32]. Among these materials, magnetic-responsive materials can be programed to bend, fold, and deform in specific ways when exposed to magnetic fields and can be used to create bioinspired robotic devices that mimic animal swimming behaviors [33–38]. One effective way to mimic the swimming or flying behavior of animals and study the effects of different flexion angles on propulsion efficiency is by creating magnetic-responsive materials capable of multimodal deformations that can break the deformation symmetry through a combination of rigid body rotation (or folding) and elastic deformation (or bending) [37,39–44].

In addition to understanding the kinematics of flexible appendage motion, it is similarly important to quantify the fluid motion surrounding the appendage to understand the associated flow structure and generated thrust force. A small number of previous studies have employed two-dimensional flow imaging measurements around magnetic-responsive material appendages and robots [36,45,46]. However, the fluid flow around bending and folding appendages is often complex and requires three-dimensional measurements that also resolve the temporal variation. Fortunately, three-dimensional flow measurement systems, such as tomographic particle image velocimetry (tomo-PIV), have been developed in recent years [47]. Further, the tomo-PIV technique has been successfully applied to low and intermediate Reynolds number flows surrounding actively swimming organisms [48–50].

The goals of the current paper are twofold: First, the effects of the appendage flexion angle and asymmetric appendage deformation on aquatic stroke performance are assessed by studying the hydrodynamics induced by the deformation of magnetic-responsive soft materials using the tomo-PIV technique. A magnetically responsive material was manufactured with either a single actuation mode (i.e., bending in both upward and downward directions) or an asymmetric multimodal actuation (i.e., folding in the upward direction and bending in the downward direction). The flow field around the appendage with the asymmetric multimode joint is analyzed and compared with the flow field resulting from the single actuation mode. Second, the effects of asymmetry of the upward and downward stroke durations are investigated on the flow field around the appendage. Thus, the volumetric flow field is quantified for four cases to separate these effects: (1) no-joint and symmetric cycle, (2) no-joint and asymmetric cycle, (3) asymmetric joint and symmetric cycle, and (4) asymmetric joint and asymmetric cycle.

II. METHODS AND MATERIALS

The experimental setup is designed to visualize the flow field around the magnetic-responsive material appendage and quantify the velocity, vorticity, vortex structure, and viscous energy dissipation rate using the tomo-PIV technique [48]. The cameras, lasers, and test tank of the tomo-PIV system were supported by a rigid, custom frame [49]. Figure 1 illustrates the schematic of the magnetic Helmholtz coil, four cameras, two lasers, and the acrylic test tank mounted using the frame. The principle of tomo-PIV is to optically record scattered light from suspended particles in the fluid from multiple perspectives to quantify the particle position within the volume. Particle displacement is determined by comparing successive digitally constructed particle volumes to calculate the local three-dimensional velocity vector at locations in the illuminated volume.

Helmholtz coils were located above and below the test tank to generate a uniform one-dimensional magnetic field. A computer-generated voltage signal controls the magnitude and
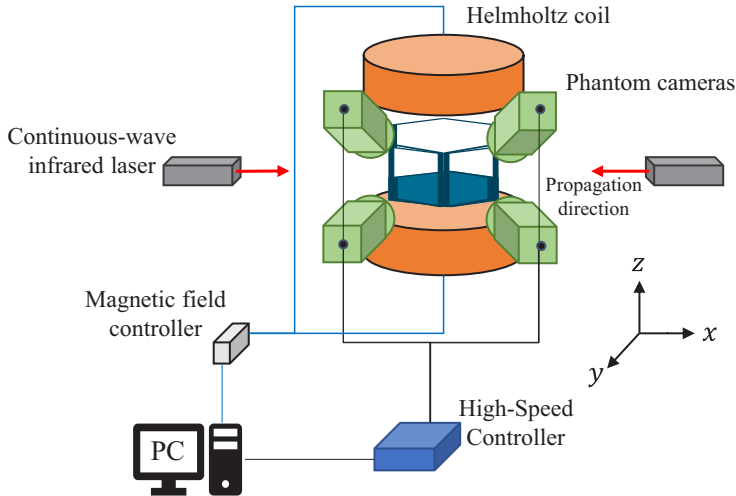
FIG. 1. Schematic of the experimental setup for the tomographic particle image velocimetry (tomo-PIV) measurements

frequency of the magnetic field. Figures 2(a) and 2(b) show the experimental time trace of the applied ±1.2 V voltage to the controller to generate a magnetic field with alternating directionality for the cases with a symmetric cycle and asymmetric cycle, respectively. The positive and negative voltages were applied for the same period of 0.1 s for the symmetric cycle. In contrast, for the
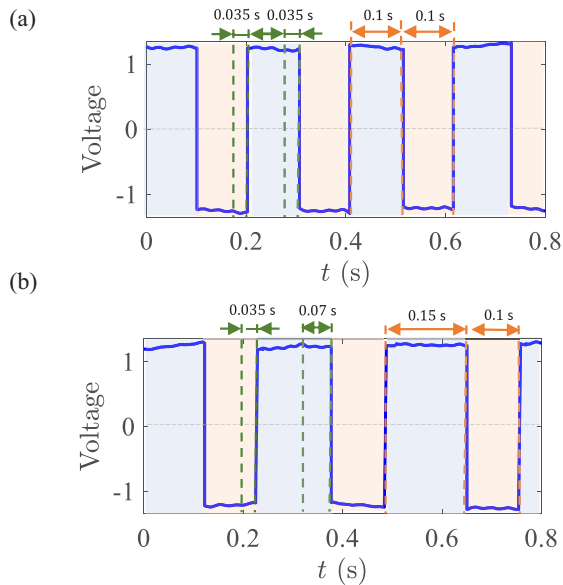
FIG. 2. Time record of the applied voltage to generate the magnetic field required for each upward (positive voltage) and downward (negative voltage) motion of the magnetic appendage for cases with (a) symmetric cycle and (b) asymmetric cycle. The green dashed line identifies the beginning of the stopping period preceding the up-to-downstroke and down-to-upstroke transitions. The light blue and orange regions correspond to the upstroke and downstroke of the appendage, respectively.
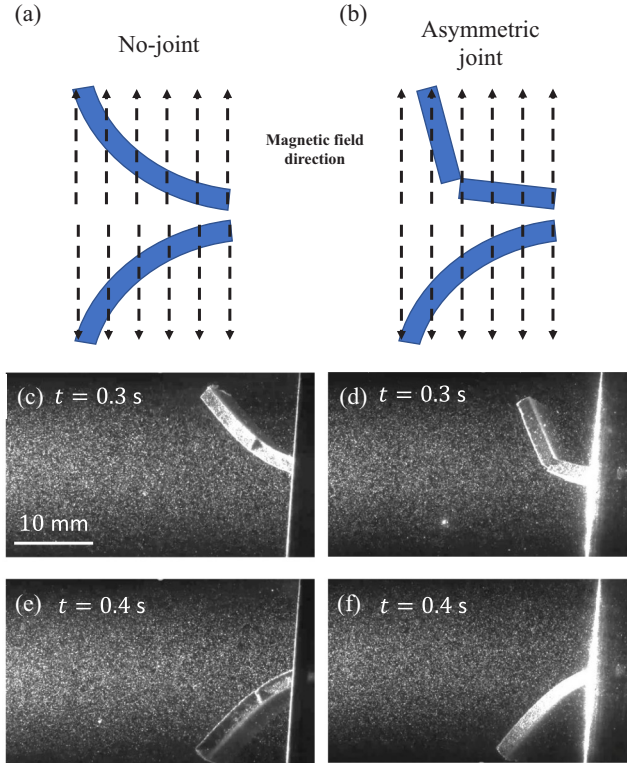
FIG. 3. Schematic of the magnetic-responsive material appendage shape with (a) no joint and (b) asymmetric joint in the middle. The raw PIV images from one of the cameras in (c), (d) the upward position and (e), (f) the downward position for cases with (c), (e) no joint and (d), (f) asymmetric joint.

asymmetric cycle, different time intervals of 0.15 s and 0.1 s were applied for each upward (positive voltage) and downward (negative voltage) motion of the magnetic-responsive material appendage, respectively.

The appendages consisted of magnetic-responsive soft material unit cells made from silicone rubber [37]. The dimensions of the appendages are 18 mm $\times$ 2 mm $\times$ 4 mm (length $\times$ thickness $\times$ width). The material unit cells were fabricated by mixing polydimethylsiloxane with NdFeB microparticles with a volume fraction of 20% (shear modulus of 164 kPa and magnetization of 109 kA/m). The mixture was oven cured. These soft materials are strongly responsive to the magnetic field due to the programed magnetization along the longitudinal direction, which can cause a substantial mechanical deformation by the exerted magnetic torque [51]. The appendage was attached at one end so the free end could deform and move in response to the magnetic field. Figures 3(a), 3(c), and 3(e) show the appendage without a joint at the peak of the upward (recovery stroke) and downward (power stroke) motions. The magnetic field in the case without an appendage joint leads to the symmetrical single-mode bending deformation in the upward [Fig. 3(c)] and downward [Fig. 3(e)] directions. A symmetry-breaking concept is implemented in the appendage to generate multimodal actuation by creating an asymmetric joint in the middle. The appendage for the cases with an asymmetric joint are shown in Figs. 3(b), 3(d), and 3(f). In this case, the multimodal actuation is achieved under switching magnetic field directions by generating motion that is more closely described as folding and rigid body rotation in the upward motion (recovery stroke) and elastic deformation (or bending) in the downward motion (power stroke) of the appendage.
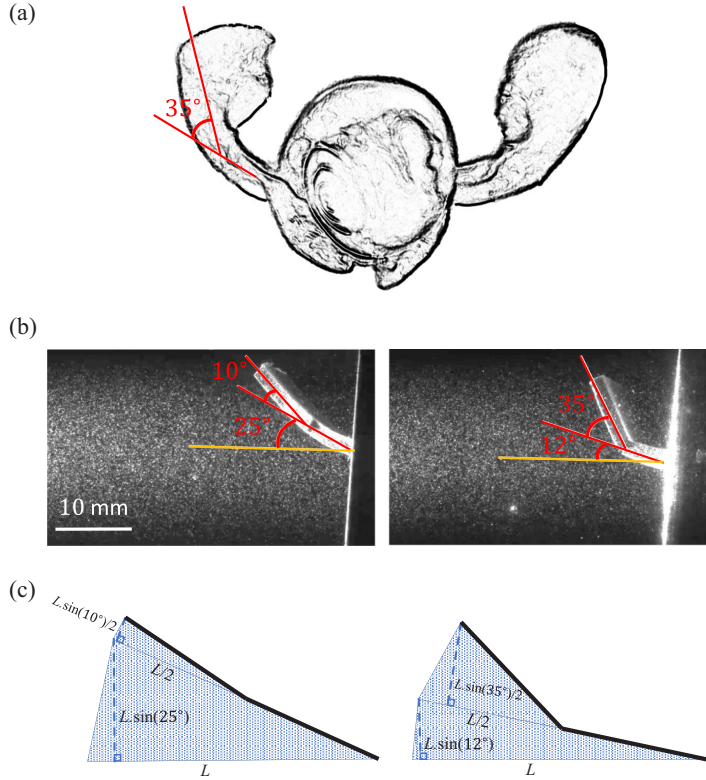
FIG. 4. The maximum appendage flexion angle of (a) a shelled Antarctic pteropod (*Limacina helicina antarctica*) and (b) the magnetic-responsive material appendage (left: no joint, right: asymmetric joint) at the peak of the upward motion. (c) The swept area of the magnetic-responsive material appendage (left: no joint, right: asymmetric joint) at the peak of the upward motion. The pteropod image is directly extracted from the recording of a swimming specimen [58].

A hexagonal transparent acrylic tank was filled with filtered water and seeded with 20 μm polyamide particles (Orgasol 2002 D NAT 1, Arkema Inc.) with an average seeding density of 0.07 particles per pixel. These particles are nearly neutrally buoyant and faithfully track the fluid motion. Two 7 W infrared continuous-wave lasers (CrystaLaser Inc.) with a wavelength of 808 nm illuminated the measurement volume from opposite sides of the tank to avoid illumination shadowing around the appendage. The height (z) and thickness (y) of the overlapped volume illumination by the lasers were 19 mm and 13 mm, respectively. The images were recorded using four high-speed one megapixel CMOS cameras (Vision Research Inc. Phantom v210; 1280×800 pixels) at 300 fps. Each camera was fitted with a Scheimpflug mount (LaVision GmbH) and a 105 mm lens (Nikon Micro-NIKKOR). As shown in Fig. 1, each camera was mounted to provide a unique viewing angle that was approximately $30°$ relative to the perpendicular viewing axis.

The tomo-PIV processing was performed in several steps. First, the cameras were calibrated and a preliminary mapping function was computed using the calibration plate images corresponding to six positions along the out-of-plane direction (i.e., y axis). The preliminary mapping function was corrected using a self-calibration procedure to reduce disparity errors [52]. The appendage was digitally masked using the MLOS algorithm and a visual hull technique was used to remove the effect of the appendage on the tomo-PIV processing [53]. Then, the MART algorithm in DaVis 8.4 (LaVision GmbH) was implemented to digitally reconstruct the three-dimensional particle volume. The three-dimensional velocity vector maps were computed by applying an iterative
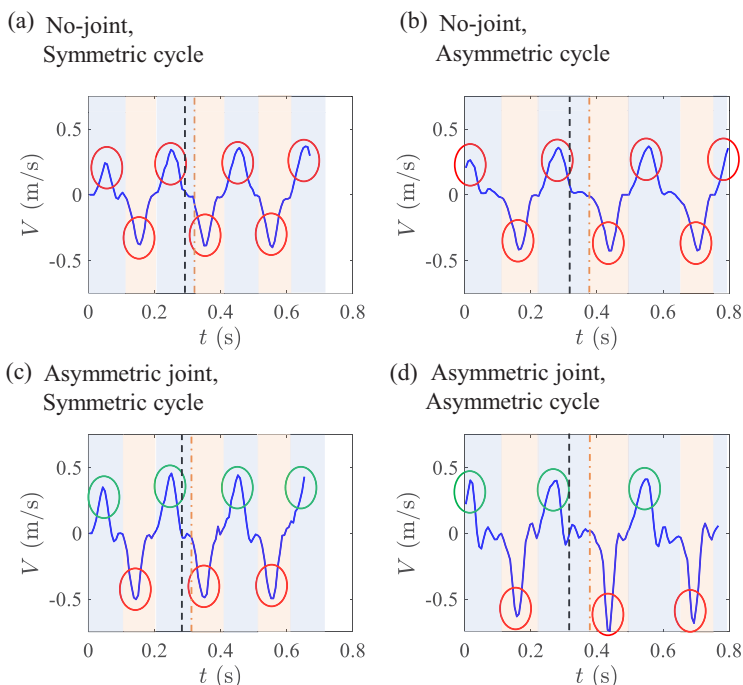
FIG. 5. Time records of the magnetic-responsive material appendage tip velocity for cases with (a) no-joint and symmetric cycle, (b) no-joint and asymmetric cycle, (c) asymmetric joint and symmetric cycle, and (d) asymmetric joint and asymmetric cycle. The red and green ovals identify the time points of greatest appendage tip velocity while bending and folding, respectively. The black dashed line and the orange dash-dotted line identify the beginning and end of the stopping period of the second cycle, respectively. The stopping periods are also identified in Fig. 2. The light blue and orange regions correspond to the upstroke and downstroke of the appendage, respectively, as also shown in Fig. 2.

three-dimensional cross-correlation technique. Three passes were made until the final smallest interrogation volume size of $32 \times 32 \times 32$ voxels with 75% overlap, which yields a final vector spacing resolution of 0.21 mm.

The appendage kinematics, i.e., the velocity of the tip, were computed using the average of the three-dimensional locations of the points along the tip of the appendage calculated from the visual hull analysis. From the tomo-PIV velocity measurements ($\vec{u}$), vorticity was calculated using $\vec{\omega} = \frac{1}{2}(\vec{\nabla} \times \vec{u})$, where derivatives were calculated by central finite difference. The quantity Q is the second invariant of the velocity gradient tensor, which is computed using $Q = \frac{1}{2}(||\overline{\overline{\Omega}}||^2 - ||\overline{\overline{S}}||^2)$. Here, $\overline{\overline{\Omega}} = [\vec{\nabla}\vec{u} - \vec{\nabla}\vec{u}^T]/2$ and $\overline{\overline{S}} = [\vec{\nabla}\vec{u} + \vec{\nabla}\vec{u}^T]/2$ are the antisymmetric (rotation) and symmetric (strain-rate) parts of the velocity-gradient tensor [54–56]. The Q-criterion defines a vortex structure as a continuous region where $Q > 0$. Notably, Menon and Mittal [55] highlighted the direct connection between Q and the dynamic pressure field via the pressure Poisson equation for incompressible flows, given by $\nabla^2 P \equiv 2\rho Q$, where P denotes pressure and ρ is the fluid density. Moreover, contrasting the vorticity and Q fields facilitates a comprehensive understanding of the overall rotational dynamics of the fluid flow. Vorticity captures local rotation effects and also identifies regions of fluid shear, whereas the Q criterion selectively isolates rotation-dominant regions by eliminating the shear contributions. Thus, the Q criterion is a valuable tool for identifying and examining vortex structures. In addition, the total viscous energy dissipation rate, ϕ, is calculated

(a) $t = 0.285$ s
No-joint, Symmetric cycle

(b) $t = 0.385$ s
No-joint, Symmetric cycle

(c) $t = 0.285$ s
Asymmetric joint, Symmetric cycle

(d) $t = 0.385$ s
Asymmetric joint, Symmetric cycle
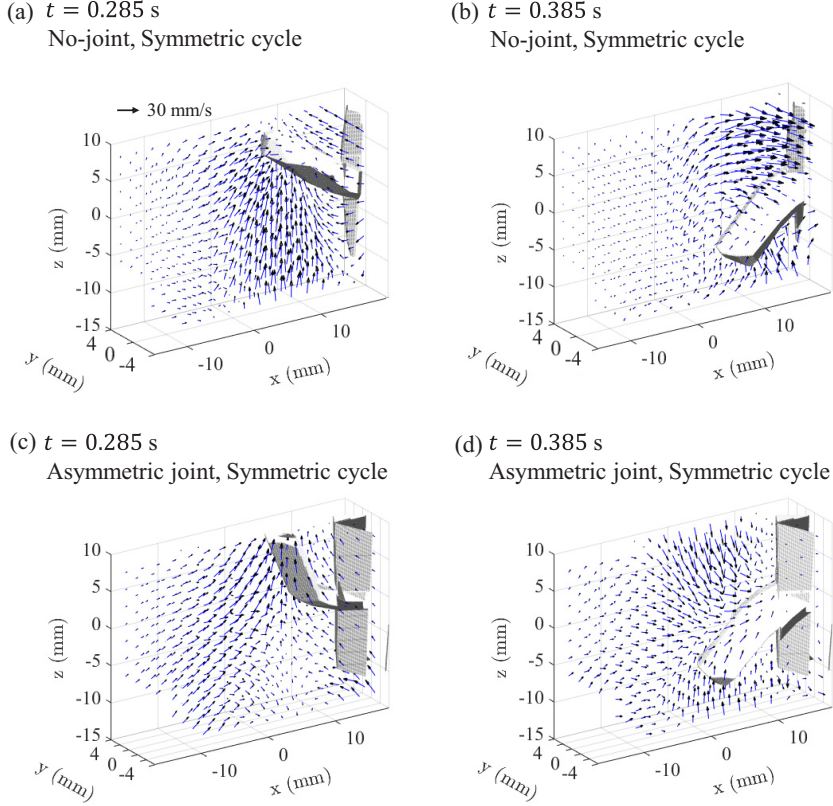
FIG. 6. Velocity vector field in the volume surrounding the appendage for cases with (a), (b) no-joint and symmetric cycle and (c), (d) asymmetric joint and symmetric cycle at the beginning of the stopping period at the peak of (a), (c) the upward motion ($t = 0.285$ s) and the peak of (b), (d) the downward motion ($t = 0.385$ s). One-eighth of all vectors are shown for clarity.

based on the velocity gradients in all directions using the three-dimensional velocity measurements and integrating over the volume [48,50],

$$\phi = \iiint \mu \left[2 \left[\left(\frac{\partial \vec{u}_x}{\partial x} \right)^2 + \left(\frac{\partial \vec{u}_y}{\partial y} \right)^2 + \left(\frac{\partial \vec{u}_z}{\partial z} \right)^2 \right] + \left(\frac{\partial \vec{u}_x}{\partial y} + \frac{\partial \vec{u}_y}{\partial x} \right)^2 + \left(\frac{\partial \vec{u}_x}{\partial z} + \frac{\partial \vec{u}_z}{\partial x} \right)^2 \right.$$
$$\left. + \left(\frac{\partial \vec{u}_y}{\partial z} + \frac{\partial \vec{u}_z}{\partial y} \right)^2 \right] dV, \tag{1}$$

where μ is the dynamic viscosity.

III. BIOINSPIRATION

The design of the magnetic-responsive material appendages was inspired by the flexion angles of appendages of a wide range of organisms with replicable patterns of propulsor bending and folding. Lucas *et al.* [9] found that maximum flexion angle among 59 species was in the range of 20º to 40º with an average of 27º. Larger than average maximum flexion angles were found for several types of fish and molluscs, like pteropods, and smaller than average angles were found for insects. For the current study, the design of the magnetic-responsive material appendages was inspired specifically by the parapodia (i.e., wing) flexion angle exhibited by the shelled Antarctic pteropod (*Limacina*

(a) $\omega_y = \pm 7$ (1/s), $t = 0.285$ s
No-joint, Symmetric cycle

(b) Q = 0.1 (1/s^2), $t = 0.285$ s
No-joint, Symmetric cycle

(c) $\omega_y = \pm 7$ (1/s), $t = 0.385$ s
No-joint, Symmetric cycle

(d) Q = 0.1 (1/s^2), $t = 0.385$ s
No-joint, Symmetric cycle
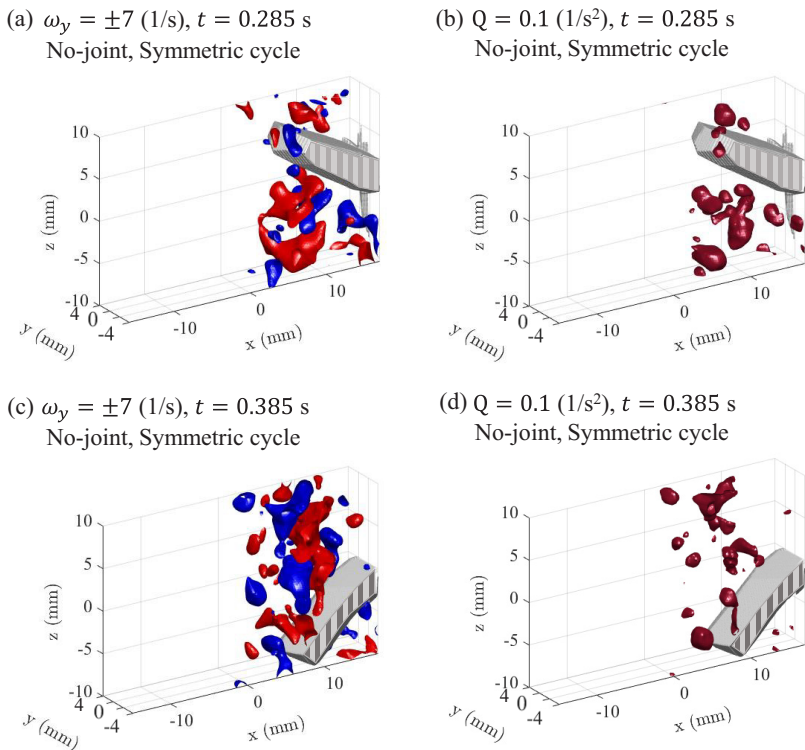
FIG. 7. The flow field (a), (b) at the peak of the upward motion ($t = 0.285$ s) and (c), (d) at the peak of the downward motion ($t = 0.385$ s) of the second cycle at the beginning of the stopping period for the case with no-joint and symmetric cycles. (a), (c) The isosurface of the y component of vorticity ($\omega_y = \pm 7$ (1/s)) and (b), (d) the isosurface of $Q = 0.1$ (1/s^2).

helicina antarctica), an animal with an intricate flapping parapodia motion to propel their body at intermediate Reynolds number [49,57–59]. Figure 4 shows the comparison between the maximum flexion angle of the pteropod parapodia and the magnetic-material appendage at the peak of the upward motion. The organism image is extracted directly from the digital recording of a swimming pteropod [58]. Following the method described by Lucas *et al.* [9], the flexion angle is computed as the angle between the line from the appendage base to the flexion point and the line from the flexion point to the tip of the appendage. The flexion angle of the magnetic-responsive material appendage with the asymmetric joint in the upward folded shape [Fig. 4(b). right image] is almost identical to the flexion angle of the pteropod parapodia at approximately 35º. In contrast, the maximum flexion angle for the appendage without a joint (approximately 10º) is smaller than the angle for the pteropod parapodia [Fig. 4(b), left image].

IV. RESULTS AND DISCUSSION

The tip velocity of the magnetic-responsive material appendage was computed as the first step in investigating the effect of the symmetry-breaking mechanisms on stroke performance. Figure 5 shows the time records of the tip velocity of the appendage for all four cases. The applied magnetic field strength was identical during all four cases; hence, the observed differences can be attributed to the morphology and cycle differences. For cases without a joint (i.e., bending motion in both directions), the tip velocity of the appendage is symmetrical and almost identical during the upward recovery and downward power strokes. However, for the case with an asymmetric joint and
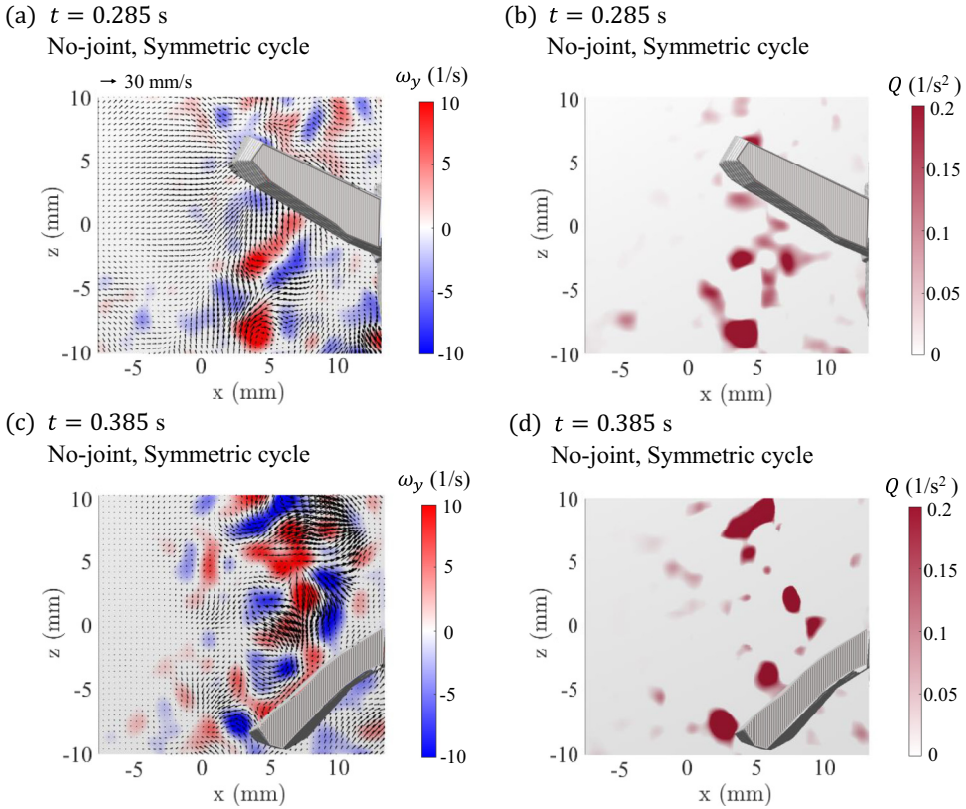
FIG. 8. The midplane field of (a), (c) the y component of vorticity overlaid with the velocity vectors and (b), (d) $Q > 0$ for (a), (b) the peak of the upward motion ($t = 0.285$ s) and (c), (d) the peak of the downward motion ($t = 0.385$ s) of the second cycle at the beginning of the stopping period for the case with no-joint and symmetric cycles.

symmetric cycle, the maximum tip velocity during the downward power stroke is roughly 1.3 times greater than the cases without a joint [Fig. 5(c)]. The difference in tip velocity during the power stroke is even greater for the asymmetric joint and asymmetric cycle case [Fig. 5(d)], where the appendage tip reaches a velocity roughly 1.8 times faster than the cases with only bending motions.

To better understand the effects of the symmetry-breaking mechanism on the flow field around the appendage, the volumetric velocity vector field is analyzed at the beginning of the stopping period, in the upward and downward directions, respectively (Fig. 6). For the upward appendage motion without a joint [Fig. 6(a)], the appendage pulls fluid located below it upward, generating strong velocity gradients. This is evident from the large velocity vectors pointing upward and with a flow component in the y-coordinate direction as well. In contrast, the folding appendage geometry during upward motion [Fig. 6(c)] generates a different flow structure. Due to the folding motion, the flow is pulled upward in front of the appendage tip instead of below it. Thus, the location of strongest velocity gradients is observed around the folding point and the tip of the appendage. During the downward motion, the appendage without a joint disrupts the strong stopping vortex generated during the upward motion [Fig. 6(b)]. This generates strong velocity gradients with orientations in all directions. In addition, the fluid turns around the appendage with strong motion in the out-of-plane direction (y direction) due to the (previous) strong upward motion of the flow. For the asymmetric joint case, the relatively weak stopping vortex and undisturbed fluid below the

(a) $\omega_y = \pm 7$ (1/s), $t = 0.285$ s
Asymmetric joint, Symmetric cycle

(b) Q = 0.1 (1/s^2), $t = 0.285$ s
Asymmetric joint, Symmetric cycle

(c) $\omega_y = \pm 7$ (1/s), $t = 0.385$ s
Asymmetric joint, Symmetric cycle

(d) Q = 0.1 (1/s^2), $t = 0.385$ s
Asymmetric joint, Symmetric cycle
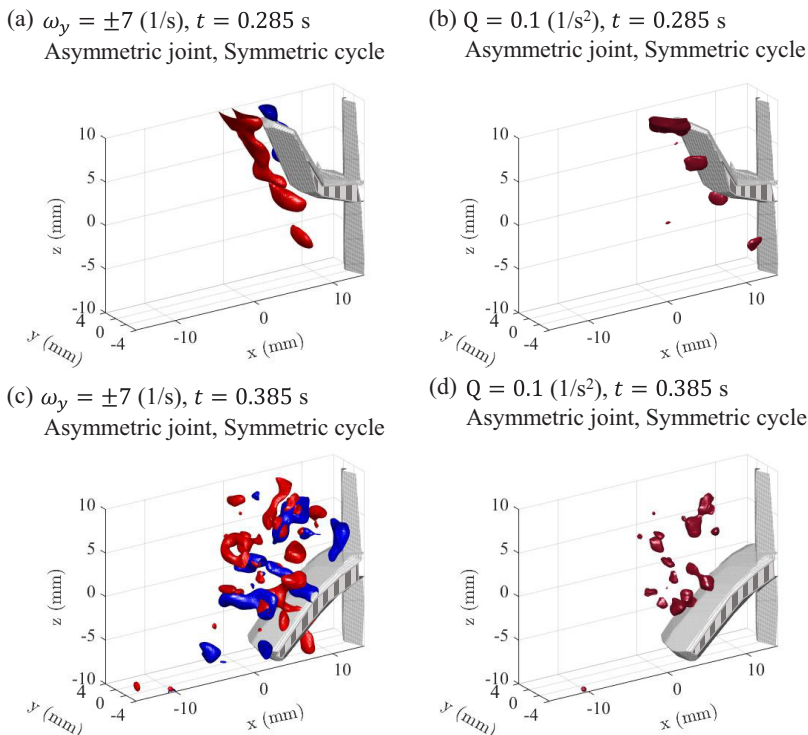
FIG. 9. The flow field (a), (b) at the peak of the upward motion ($t = 0.285$ s) and (c), (d) at the peak of the downward motion ($t = 0.385$ s) of the second cycle at the beginning of the stopping period for the case with an asymmetric joint and symmetric cycle. (a), (c) The isosurface of the y component of vorticity [$\omega_y = \pm 7$ (1/s)] and (b), (d) the isosurface of $Q = 0.1$ (1/s^2).

appendage provide less disruption to the downward appendage motion [Fig. 6]. Consequently, the strength of the generated velocity gradients is less in this case.

Figures 7–10 show three-dimensional isosurfaces of the y component of vorticity and Q and the midplane (i.e., the plane located at the midpoint of the transverse dimension of the appendage) fields at the peak of the upstroke and downstroke motion for the no-joint case (Figs. 7 and 8) and asymmetric joint case (Figs. 9 and 10). In the panels showing the three-dimensional isosurfaces, a value of $Q = 0.1$ (1/s^2) was selected because this value best visualized the vortex structures and differences between cases.

The appendage with no-joint generates regions of strong positive and negative vorticity during the upward bending motion [Figs. 7(a) and 8(a)]. The midplane field of velocity vectors overlaying adjacent positive and negative vorticity regions illustrates that the appendage motion induces a blend of rotation regions and shear layers in the flow field. This observation is confirmed through the midplane field and three-dimensional isosurface representations of Q [Figs. 7(b) and 8(b)]. While regions of elevated vorticity exist beneath the appendage, the diminished prevalence of $Q > 0$ regions compared to the vorticity field signifies the substantial role played by shear in the flow and the general lack of coherence in the vortex structures. During the downward bending motion, the appendage disrupts the flow structure generated during the upstroke, resulting in a significant flow disturbance [Figs. 7(c) and 8(c)]. Regions of strong vorticity (of both signs) and vortex structure (as indicated by $Q > 0$ regions) are more pronounced during the downstroke [Figs. 7(c), 7(d), 8(c), and 8(d)] in comparison to the upstroke motion.
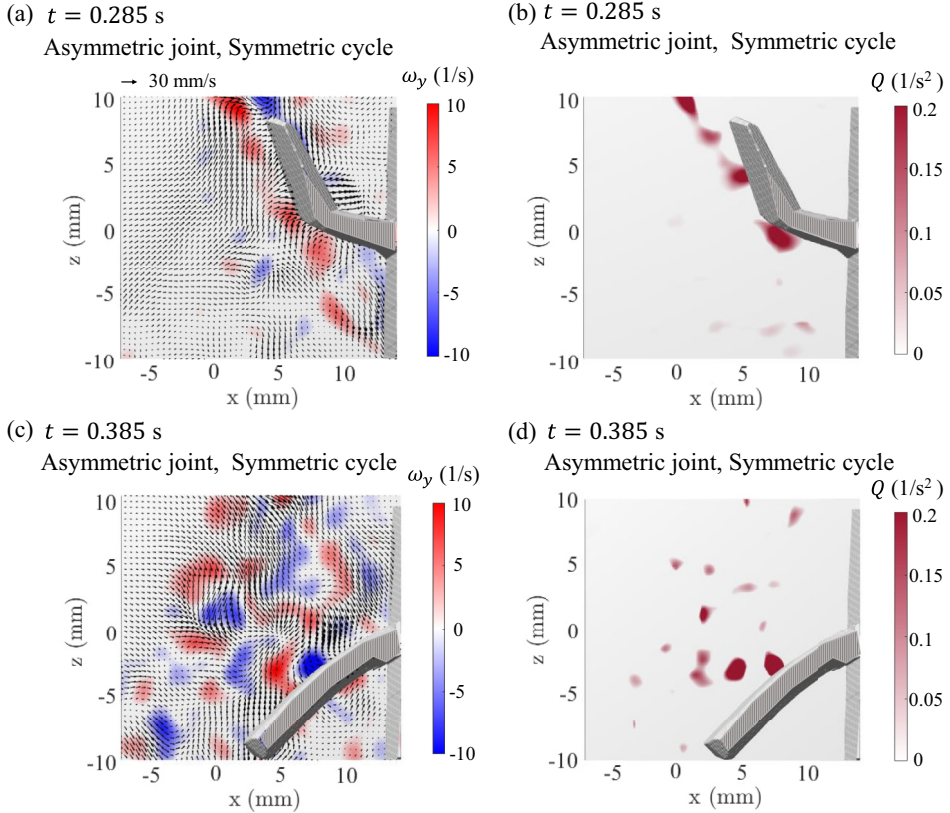
FIG. 10. The midplane field of (a), (c) the y component of vorticity overlaid with the velocity vectors and (b), (d) $Q > 0$ for (a), (b) the peak of the upward motion ($t = 0.285$ s) and (c), (d) the peak of the downward motion ($t = 0.385$ s) of the second cycle at the beginning of the stopping period for the case with an asymmetric joint and symmetric cycle.

A distinctly different flow pattern emerges for the appendage with multimodal deformation, as depicted in Figs. 9, and 10. During the upward folding motion, the midplane field of velocity vectors, combined with the vorticity and Q fields, reveal that the appendage tip draws flow from the front side towards the appendage, with minimal disturbance below the appendage [(Figs. 9(a), 9(b), 10(a), and 10(b)]. The most significant flow disturbance occurs along the tip of the appendage and near the joint, and the regions of elevated vorticity are notably reduced compared to those observed during the upstroke for the no-joint appendage. Moreover, the Q field reveals the generation of small vortex structures exclusively near the joint and the tip of the appendage [Figs. 9(b) and 10(b)]. During the downward bending motion, similar patterns of vorticity and vortex structures to those produced during downward motion in the no-joint case appear above the appendage [Figs. 9(c) and 10(c)]. However, the strength of the structures is considerably reduced due to fewer disturbances remaining from the folding upstroke motion [Figs. 9(c), 9(d), 10(c), and 10(d)].

To gain a deeper understanding of the influence of the symmetry-breaking mechanism and the stopping period, the vorticity magnitude ($|\omega| = \sqrt{\omega_x^2 + \omega_y^2 + \omega_z^2}$) field surrounding the magnetic-responsive material appendage is analyzed. Figures 11 and 12 present isosurfaces of vorticity magnitude at the beginning (first row) and end (second row) of the stopping period at the peak of the upstroke and downstroke, respectively. It is important to note that a unique isocontour value is plotted at the end of the stopping period due to the rapid dissipation of vorticity during the stopping
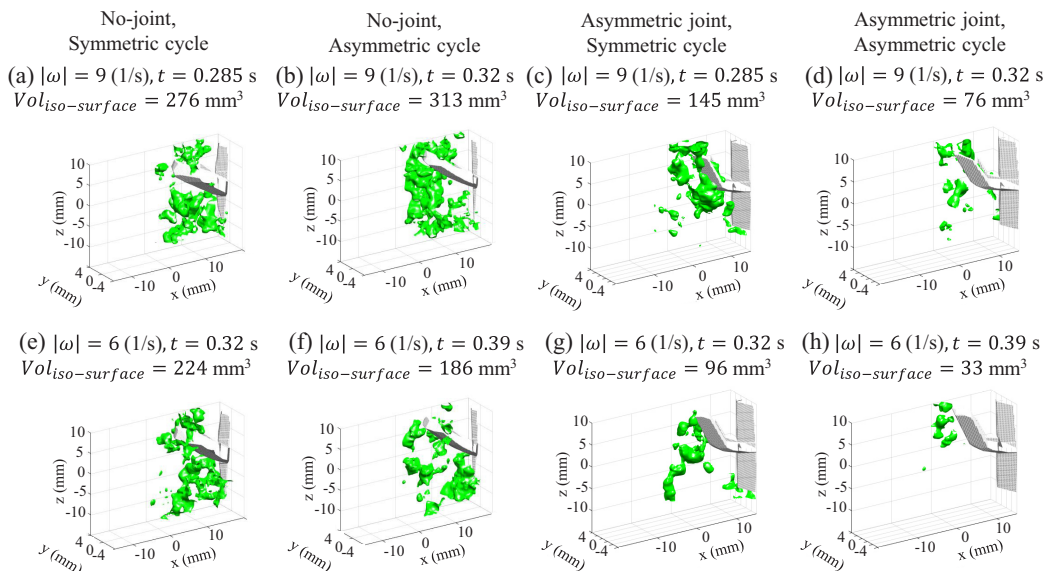
FIG. 11. (a)–(d) The isosurface of the absolute value of vorticity [$|\omega| = 9$ (1/s)] at the peak of the upward motion of the second cycle at the *beginning* of the stopping period ($t = 0.285$ s and $t = 0.32$ s for the cases with symmetric and asymmetric cycles, respectively). (e)–(h) The isosurface of the absolute value of vorticity [$|\omega| = 6$ (1/s)] at the peak of the upward motion of the second cycle at the *end* of the stopping period ($t = 0.32$ s and $t = 0.39$ s for the cases with symmetric and asymmetric cycles, respectively). The isosurfaces are for cases with (a), (e) no-joint and symmetric cycle; (b), (f) no-joint and asymmetric cycle; (c), (g) asymmetric joint and symmetric cycle; and (d), (h) the asymmetric joint and asymmetric cycle.

period (otherwise minimal structure appears in the figure). For the upward (downward) bending deformation of the no-joint appendage [Figs. 11(a), 11(b), 11(e), 11(f), 12(a), and 12(c)], regions of elevated vorticity magnitude are observed throughout the region below (above) the appendage. In contrast, for the rigid-body appendage rotation of the asymmetric joint case, the regions of elevated vorticity are prominent near the tip and joint locations [Figs. 11(c), 11(d), 11(g), 11(h), 12(b), and 12(d)].

The effect of the stopping period is observed by comparing the first row to the second row in Figs. 11 and 12. During the stopping period, dissipation acts to reduce the regions of elevated vorticity formed during the upward (or downward) appendage motion. However, the extent of dissipation varies among the cases depending on the duration of the stopping period. Specifically, cases with an asymmetric cycle (and a longer interstroke interval) exhibit greater reduction of the regions of elevated vorticity [Figs. 11(b) vs 11(f), and 11(d) vs 11(h)], which is supported by the volume of the elevated vorticity region reported in the figure panels. The flow disturbance and regions of elevated vorticity remaining in the flow after the stopping period act as flow resistance against the appendage motion during the next downward power stroke. Thus, increasing the stopping period can effectively decrease the flow resistance and enhance stroke performance during the subsequent downward power stroke.

Flow resistance in this context is a result of the dynamic interplay between the appendage and the fluid flow, which involves both inertial and viscous effects. Inertial effects are associated with the momentum of the fluid opposing the appendage as it moves through the flow disturbance. On the other hand, viscous effects come into play due to the frictional interaction between the fluid flow and the appendage surface. Moving through the flow disturbance leads to enhanced velocity

No-joint,
Symmetric cycle

Asymmetric joint,
Symmetric cycle

(a) $|\omega| = 9$ (1/s), $t = 0.385$ s
$Vol_{iso-surface} = 414$ mm³

(b) $|\omega| = 9$ (1/s), $t = 0.385$ s
$Vol_{iso-surface} = 134$ mm³

(c) $|\omega| = 6$ (1/s), $t = 0.42$ s
$Vol_{iso-surface} = 191$ mm³

(d) $|\omega| = 6$ (1/s), $t = 0.42$ s
$Vol_{iso-surface} = 41$ mm³
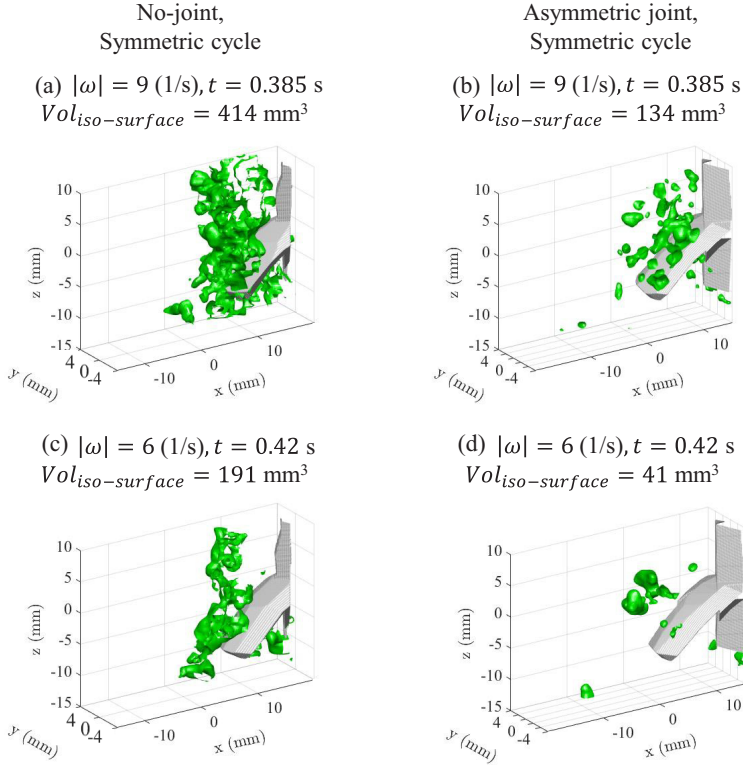
FIG. 12. (a), (b) The isosurface of the absolute value of vorticity [$|\omega| = 9$ (1/s)] at the peak of the downward motion of the second cycle at the *beginning* of the stopping period ($t = 0.385$ s). (c), (d) The isosurface of the absolute value of vorticity [$|\omega| = 6$ (1/s)] at the peak of the downward motion of the second cycle at the *end* of the stopping period ($t = 0.42$ s). The isosurfaces are for cases with (a), (c) no-joint and symmetric cycle and (b), (d) asymmetric joint and symmetric cycle.

gradients, leads to elevated viscous dissipation of energy, and contributes to the overall resistance against the appendage motion.

To further quantify the differences between these cases, the time records of the volumetric average of the enstrohpy ($\varepsilon = |\omega|^2$) and the total viscous energy dissipation rate are shown in Figs. 13 and 14, respectively. The strength of the vorticity field and the viscous dissipation rate during the upward motion of the first cycle are smaller than the subsequent cycles because of the transient start-up of the flow. After the first cycle of each case, the flow behavior is more consistently repeated in subsequent cycles. During each upward or downward stroke of the appendage, the maximum value of enstrophy and viscous dissipation rate occurs at an intermediate point of each stroke period. The formed regions of elevated vorticity partially dissipate during the stopping period between each upward and downward stroke. Comparison to the time record of appendage tip velocity (Fig. 5) reveals that the appendage velocity during the downstroke is inversely connected to the enstrophy at the start of the downstroke. This relationship suggests, as noted above, the remaining regions of elevated vorticity from each stroke period acts as resistance against the motion of the appendage during the next stroke. Given the convoluted nature of the vorticity field (Figs. 11 and 12), the presence of regions of elevated vorticity appear to serve as resistance to the appendage motion, rather than a benefit as has been observed in some instances of coherent vortex structure shedding (e.g., Ahlborn *et al.* [60]).
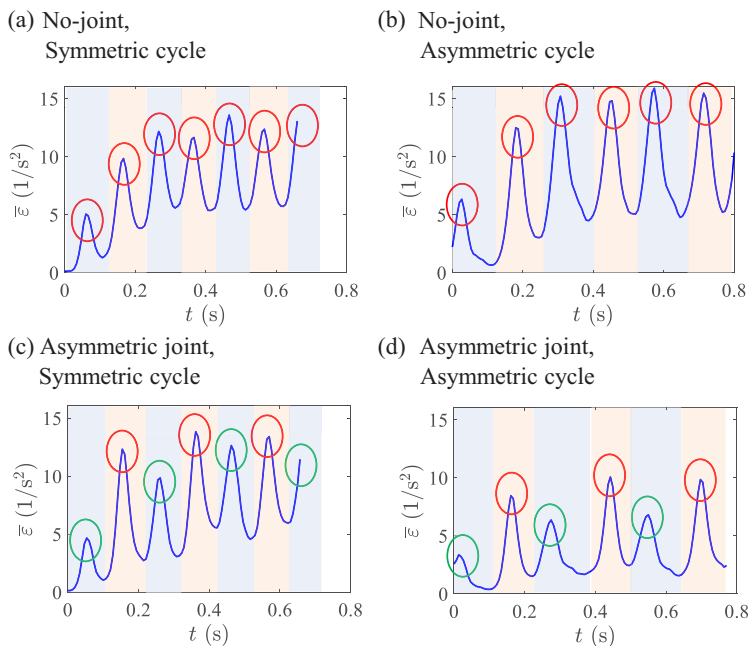
FIG. 13. Time records of the volumetric average of the enstrophy for cases with (a) no-joint and symmetric cycle, (b) no-joint and asymmetric cycle, (c) asymmetric joint and symmetric cycle, and (d) asymmetric joint and asymmetric cycle. The red and green ovals identify the time-points of greatest appendage tip velocity while bending and folding, respectively (see Fig. 5). The light blue and orange regions correspond to the upstroke and downstroke of the appendage, respectively.

The volume-averaged enstrophy and viscous dissipation rate is almost equal during the upward and downward strokes for the no-joint cases [i.e., comparing sequential peak values in Figs. 13(a) and 13(b) and Figs. 14(a) and 14(b)]. However, the minimum points in the time records, which correspond to the stopping periods, are smaller for the case with an asymmetric cycle [Figs. 13(b) and 14(b)] compared to the case with a symmetric cycle [Figs. 13(a) and 14(a)]. This difference occurs because of greater dissipation of the vorticity and diminished velocity gradients following the longer stopping period between recovery and power strokes.

By adding the appendage joint, the symmetry of the generated flow structure is broken during the power and recovery strokes [Figs. 13(c), 13(d) 14(c), and 14(d)]. During the downward power stroke with bending deformation (i.e., noted with red circles), the maximum enstrophy and viscous dissipation rate are approximately 1.4 times greater than the maximum values during the upward recovery stroke with folding deformation (i.e., noted with green circles). This observation can be explained by the fact that the swept volume of the appendage is smaller in the upward folding motion, which leads to less flow resistance against the appendage motion and, thus, smaller peak values of enstrophy and viscous dissipation rate. The swept volume for the bending and folding cases can be estimated from Fig. 4(c) using $WL^2(\sin(25°)/2 + \sin(10°)/8)$ and $WL^2(\sin(12°)/2 + \sin(35°)/8)$, respectively, where L is the total length and W is the width of the appendage. Consistently, the estimated swept volume of the bending geometry is also roughly 1.2–1.3 times greater than the case with the folding appendage geometry.

The appendage joint also alters the peak and trough values of enstrophy and viscous dissipation rate. The peak and trough values are roughly 1.4 times greater for the bending motion compared to the folding motion [comparison between Figs. 13(a) and 14(a) with Figs. 13(c) and 14(c), respectively]. This difference is amplified when incorporating the asymmetric cycle [comparison
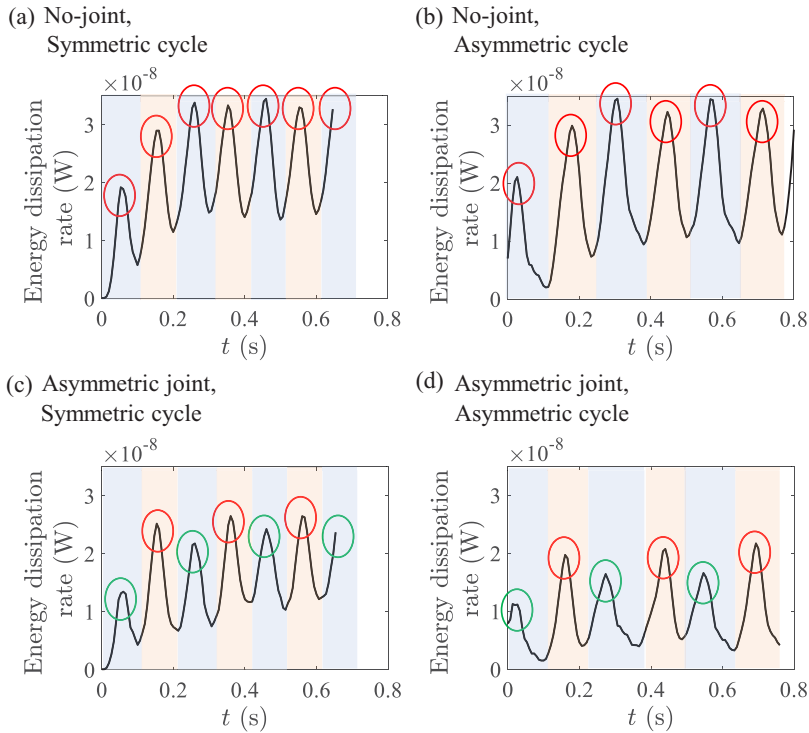
FIG. 14. Time records of the total viscous energy dissipation rate for cases with (a) no-joint and symmetric cycle, (b) no-joint and asymmetric cycle, (c) asymmetric joint and symmetric cycle, and (d) asymmetric joint and asymmetric cycle. The red and green ovals identify the time points of greatest appendage tip velocity while bending and folding, respectively (see Fig. 5). The light blue and orange regions correspond to the upstroke and downstroke of the appendage, respectively.

between Figs. 13(b) and 14(b) with Figs. 13(d) and 14(d), respectively], where the peak and trough values of enstrophy and viscous dissipation rate are roughly 1.9 times greater for the upward bending motion case. The enhanced difference shows that the effect of an asymmetric joint and an asymmetric cycle together can reduce the strength of the vorticity field and the flow resistance during the power stroke, which leads to faster appendage motion during the downward power stroke and improved stroke performance.

It is instructive to consider the flow-field results relative to the biological flows that inspired the appendage design. For instance, pteropods and manta rays generate leading-edge vortices on their appendages that are critical to generate thrust [49,61]. In the case of manta rays, the leading-edge vortices adhere to the tip of the wing during upward folding motion and eventually enhance thrust generation [61]. While some flow features are similar, direct comparisons are challenging since the biological appendages consist of complex 3D morphology and motions. Nevertheless, the double vortex structures along the appendage (around the tip and the middle of the appendage) during downward bending motion [Figs. 8(d) and 10(d)] are similar to the leading and trailing edge vortex structures observed during the downstroke of bat wings [62]. In bats, these vortex structures develop due to the pressure difference between the upper and lower surfaces of the appendage (i.e., wing). As the appendage moves downward, the fluid flowing over the upper surface accelerates, creating a region of low pressure. At the same time, the fluid flowing under the appendage moves at a slower

speed and generates higher pressure. This pressure difference causes flow separation from the edge of the appendage, which creates a swirling motion that forms a vortex structure.

V. CONCLUSIONS

The symmetry-breaking mechanism inspired by flapping swimming animals, such as pteropods, was investigated by designing magnetic-responsive material appendages that can undergo two distinct shape changes when subjected to an identical external unidirectional magnetic field: symmetric elastic deformation (or bending) motion in both directions or an asymmetric joint with bending during the downward power stroke and rigid body rotation (or folding) during the upward recovery stroke. The appendage tip velocity in the downward bending direction for the cases with an asymmetric joint was 1.3 to 1.8 times faster compared to those without a joint.

The greater appendage velocity for the cases with an asymmetric joint is explained by considering the velocity, vorticity, vortex structures, and total viscous dissipation rate of the induced flow. For the appendage with multimodal motion, the vorticity, vortex structures, and total viscous dissipation rate are reduced during the upward motion compared to the no-joint appendage case due to the reduced swept volume for the folding appendage motion. The reduced strength of the flow disturbance during the upward recovery stroke leads to less flow resistance and increased appendage velocity during the downward power stroke.

Similarly, breaking the cycle symmetry extends the brief stopping period at the top of the upward motion of the recovery stroke. During the stopping period, the vorticity field and velocity gradients partially dissipate, which reduces the flow resistance and increases the appendage velocity during the downward power stroke.

The conclusion is that the multimode appendage motion and the asymmetric flapping stroke cycle can reduce the strength of the vorticity field in the fluid surrounding the appendage and viscous energy dissipation during the downward power stroke, which leads to faster motion of the appendage and, thus, more effective swimming propulsion. These magnetic-responsive soft materials have the potential to revolutionize the field of underwater propulsion and create opportunities for exploration and discovery in aquatic environments.

ACKNOWLEDGMENTS

---

[1] S. A. Combes and T. L. Daniel, Shape, flapping and flexion: Wing and fin design for forward flight, J. Exp. Biol. **204**, 2073 (2001).

[2] F. E. Fish, L. E. Howle, and M. M. Murray, Hydrodynamic flow control in marine mammals, Integr. Comp. Biol. **48**, 788 (2008).

[3] G. Liu, Y. Ren, J. Zhu, H. Bart-Smith, and H. Dong, Thrust producing mechanisms in ray-inspired underwater vehicle propulsion, Theor. App. Mech. Lett. **5**, 54 (2015).

[4] B. J. Gemmell, S. M. Fogerson, J. H. Costello, J. R. Morgan, J. O. Dabiri, and S. P. Colin, How the bending kinematics of swimming lampreys build negative pressure fields for suction thrust, J. Exp. Biol. **219**, 3884 (2016).

[5] H. Hang, S. Heydari, J. H. Costello, and E. Kanso, Active tail flexion in concert with passive hydrodynamic forces improves swimming speed and efficiency, J. Fluid Mech. **932**, A35 (2022).

[6] M. S. Triantafyllou, G. S. Triantafyllou, and R. Gopalkrishnan, Wake mechanics for thrust generation in oscillating foils, Phys. Fluids A **3**, 2835 (1991).

[7] J. M. Anderson, K. Streitlien, D. S. Barrett, and M. S. Triantafyllou, Oscillating foils of high propulsive efficiency, J. Fluid Mech. **360**, 41 (1998).

[8] S. P. Colin, J. H. Costello, J. O. Dabiri, A. Villanueva, J. B. Blottman, B. J. Gemmell, and S. Priya, Biomimetic and live medusae reveal the mechanistic advantages of a flexible bell margin, PLoS One **7**, e48909 (2012).

[9] K. N. Lucas, N. Johnson, W. T. Beaulieu, E. Cathcart, G. Tirrell, S. P. Colin, B. J. Gemmell, J. O. Dabiri, and J. H. Costello, Bending rules for animal propulsion, Nat. Commun. **5**, 3293 (2014).

[10] J. Toomey and J. D. Eldredge, Numerical and experimental study of the fluid dynamics of a flapping wing with low order flexibility, Phys. Fluids **20**, 073603 (2008).

[11] S. Heathcote, Z. Wang, and I. Gursul, Effect of spanwise flexibility on flapping wing propulsion, J. Fluids Struct. **24**, 183 (2008).

[12] G. V. Lauder, P. G. A. Madden, R. Mittal, H. Dong, and M. Bozkurttas, Locomotion with flexible propulsors: I. Experimental analysis of pectoral fin swimming in sunfish, Bioinspir. Biomim. **1**, S25 (2006).

[13] S. Alben, Optimal flexibility of a flapping appendage in an inviscid fluid, J. Fluid Mech. **614**, 355 (2008).

[14] S. Y. Shinde and J. H. Arakeri, Physics of unsteady thrust and flow generation by a flexible surface flapping in the absence of a free stream, Proc. R. Soc. A: Math. Phys. Eng. Sci. **474**, 20180519 (2018).

[15] Q. Zhong, J. Zhu, F. E. Fish, S. J. Kerr, A. M. Downs, H. Bart-Smith, and D. B. Quinn, Tunable stiffness enables fast and efficient swimming in fish-like robots, Sci. Robot. **6**, eabe4088 (2021).

[16] S. D. Ross, Optimal flapping strokes for self-propulsion in a perfect fluid, in *2006 American Control Conference* (IEEE, Minneapolis, MN, USA, 2006), pp. 4118–4122.

[17] A. Hedenström and G. Spedding, Beyond robins: aerodynamic analyses of animal flight, J. R. Soc. Interface **5**, 595 (2008).

[18] L. Zheng, T. L. Hedrick, and R. Mittal, Time-varying wing-twist improves aerodynamic efficiency of forward flight in butterflies, PLoS One **8**, e53060 (2013).

[19] J. Y. Zhu and C. Y. Zhou, Aerodynamic performance of a two-dimensional flapping wing in asymmetric stroke, Proc. Inst. Mech. Eng. G: J. Aerosp. Eng. **228**, 641 (2014).

[20] K. Liu, H. Huang, and X. Y. Lu, Hydrodynamic benefits of intermittent locomotion of a self-propelled flapping plate, Phys. Rev. E **102**, 053106 (2020).

[21] N. Harada, T. Oura, M. Maeda, Y. Shen, D. M. Kikuchi, and H. Tanaka, Kinematics and hydrodynamics analyses of swimming penguins: Wing bending improves propulsion performance, J. Exp. Biol. **224**, jeb242140 (2021).

[22] X. Lang, B. Song, W. Yang, and X. Yang, Effect of spanwise folding on the aerodynamic performance of three dimensional flapping flat wing, Phys. Fluids **34**, 021906 (2022).

[23] W. Wang, J. Y. Lee, H. Rodrigue, S. H. Song, W. S. Chu, and S. H. Ahn, Locomotion of inchworm-inspired robot made of smart soft composite (SSC), Bioinspir. Biomim. **9**, 046006 (2014).

[24] I. Must, F. Kaasik, I. Poldsalu, L. Mihkels, U. Johanson, A. Punning, and A. Aabloo, Ionic and capacitive artificial muscle for biomimetic soft robotics, Adv. Eng. Mater. **17**, 84 (2015).

[25] H. W. Huang, M. S. Sakar, A. J. Petruska, S. Pané, and B. J. Nelson, Soft micromachines with programmable motility and morphology, Nat. Commun. **7**, 12263 (2016).

[26] M. Medina-Sánchez, V. Magdanz, M. Guix, V. M. Fomin, and O. G. Schmidt, Swimming microrobots: Soft, reconfigurable, and smart, Adv. Funct. Mater. **28**, 1707228 (2018).

[27] J. Frame, N. Lopez, O. Curet, and E. D. Engeberg, Thrust force characterization of free-swimming soft robotic jellyfish, Bioinspir. Biomim. **13**, 064001 (2018).

[28] Q. Zhao, Y. Wang, H. Cui, and X. Du, Bio-inspired sensing and actuating materials, J. Mater. Chem. C **7**, 6493 (2019).

[29] Q. Ze, S. Wu, J. Nishikawa, J. Dai, Y. Sun, S. Leanza, C. Zemelka, L. S. Novelino, G. H. Paulino, and R. R. Zhao, Soft robotic origami crawler, Sci. Adv. **8**, eabm7834 (2022).

[30] S. Wu, C. M. Hamel, Q. Ze, F. Yang, H. J. Qi, and R. R. Zhao, Evolutionary algorithm-guided voxel-encoding printing of functional hard-magnetic soft active materials, Adv. Intell. Syst. **2**, 2000060 (2020).

[31] Z. Ren, R. Zhang, R. H. Soon, Z. Liu, W. Hu, P. R. Onck, and M. Sitti, Soft-bodied adaptive multimodal locomotion strategies in fluid-filled confined spaces, Sci. Adv. **7**, eabh2022 (2021).

[32] M. Li, A. Pal, A. Aghakhani, A. Pena-Francesch, and M. Sitti, Soft actuators for real-world applications, Nat. Rev. Mater. **7**, 235 (2022).

[33] K. E. Peyer, L. Zhang, and B. J. Nelson, Bio-inspired magnetic swimming microrobots for biomedical applications, Nanoscale **5**, 1259 (2013).

[34] T. Qiu, T. C. Lee, A. G. Mark, K. I. Morozov, R. Münster, O. Mierka, S. Turek, A. M. Leshansky, and P. Fischer, Swimming by reciprocal motion at low Reynolds number, Nat. Commun. **5**, 5119 (2014).

[35] L. Yang, Q. Wang, C. I. Vong, and L. Zhang, A miniature flexible-link magnetic swimming robot with two vibration modes: Design, modeling and characterization, IEEE Robot. Autom. Lett. **2**, 2024 (2017).

[36] Z. Ren, W. Hu, X. Dong, and M. Sitti, Multi-functional soft-bodied jellyfish-like swimming, Nat. Commun. **10**, 2703 (2019).

[37] S. Wu, Q. Ze, R. Zhang, N. Hu, Y. Cheng, F. Yang, and R. Zhao, Symmetry-breaking actuation mechanism for soft robotics and active metamaterials, ACS Appl. Mater. Interfaces **11**, 41649 (2019).

[38] Z. Shen, F. Chen, X. Zhu, K. T. Yong, and G. Gu, Stimuli-responsive functional materials for soft robotics, J. Mater. Chem. B **8**, 8972 (2020).

[39] J. M. Gal and R. W. Blake, Biomechanics of frog swimming: II. Mechanics of the limb-beat cycle in *Hymenochirus Boettgeri*, J. Exp. Biol. **138**, 413 (1988).

[40] A. Villanueva, C. Smith, and S. Priya, A biomimetic robotic jellyfish (Robojelly) actuated by shape memory alloy composite actuators, Bioinspir. Biomim. **6**, 036004 (2011).

[41] T. Li, G. Li, Y. Liang, T. Cheng, J. Dai, X. Yang, B. Liu, Z. Zeng, Z. Huang, Y. Luo *et al.*, Fast-moving soft electronic fish, Sci. Adv. **3**, e1602045 (2017).

[42] T. Cheng, G. Li, Y. Liang, M. Zhang, B. Liu, T. W. Wong, J. Forman, M. Chen, G. Wang, Y. Tao *et al.*, Untethered soft robotic jellyfish, Smart Mater. Struct. **28**, 015019 (2019).

[43] W. Hu, G. Z. Lum, M. Mastrangeli, and M. Sitti, Small-scale soft-bodied robot with multimodal locomotion, Nature (London) **554**, 81 (2018).

[44] C. S. X. Ng, M. W. M. Tan, C. Xu, Z. Yang, P. S. Lee, and G. Z. Lum, Locomotion of miniature soft robots, Adv. Mater. **33**, 2003558 (2021).

[45] A. Friedman, A. Liberzon, and G. Kósa, Propulsive force of a magnetic, MRI-based swimmer, in *2015 IEEE International Conference on Robotics and Automation (ICRA)* (IEEE, Seattle, WA, USA, 2015), pp. 4736–4741.

[46] J. Zhang and E. Diller, Untethered miniature soft robots: Modeling and design of a millimeter-scale swimming magnetic sheet, Soft Robot. **5**, 761 (2018).

[47] G. E. Elsinga, F. Scarano, B. Wieneke, and B. W. van Oudheusden, Tomographic particle image velocimetry, Exp. Fluids **41**, 933 (2006).

[48] D. W. Murphy, D. R. Webster, and J. Yen, A high-speed tomographic PIV system for measuring zooplanktonic flow, Limnol. Oceanogr.: Methods **10**, 1096 (2012).

[49] D. Adhikari, D. R. Webster, and J. Yen, Portable tomographic PIV measurements of swimming shelled Antarctic pteropods, Exp. Fluids **57**, 180 (2016).

[50] A. N. Skipper, D. W. Murphy, and D. R. Webster, Characterization of hop-and-sink daphniid locomotion, J. Plankton Res. **41**, 142 (2019).

[51] R. Zhao, Y. Kim, S. A. Chester, P. Sharma, and X. Zhao, Mechanics of hard-magnetic soft materials, J. Mech. Phys. Solids **124**, 244 (2019).

[52] B. Wieneke, Volume self-calibration for 3D particle image velocimetry, Exp. Fluids **45**, 549 (2008).

[53] D. Adhikari and E. K. Longmire, Visual hull method for tomographic PIV measurement of flow around moving objects, Exp. Fluids **53**, 943 (2012).

[54] J. Jeong and F. Hussain, On the identification of a vortex, J. Fluid Mech. **285**, 69 (1995).

[55] K. Menon and R. Mittal, Significance of the strain-dominated region around a vortex on induced aerodynamic loads, J. Fluid Mech. **918**, R3 (2021).

[56] K. Menon and R. Mittal, Quantitative analysis of the kinematics and induced aerodynamic loading of individual vortices in vortex-dominated flows: A computation and data-driven approach, J. Comput. Phys. **443**, 110515 (2021).

[57] D. W. Murphy, D. Adhikari, D. R. Webster, and J. Yen, Underwater flight by the planktonic sea butterfly, J. Exp. Biol. **219**, 535 (2016).

[58] M. Mohaghar, D. Adhikari, and D. R. Webster, Characteristics of swimming shelled Antarctic pteropods (*Limacina helicina antarctica*) at intermediate Reynolds number regime, Phys. Rev. Fluids **4**, 111101(R) (2019).

[59] F. Karakas, A. E. Maas, and D. W. Murphy, A novel cylindrical overlap-and-fling mechanism used by sea butterflies, J. Exp. Biol. **223**, jeb.221499 (2020).

[60] B. Ahlborn, S. Chapman, R. Stafford, R. W. Blake, and D. G. Harper, Experimental simulation of the thrust phases of fast-start swimming of fish, J. Exp. Biol. **200**, 2301 (1997).

[61] K. W. Moored, W. Smith, J. M. Hester, W. Chang, and H. Bart-Smith, Investigating the thrust production of a myliobatoid-inspired oscillating wing, Adv. Sci. Technol. **58**, 25 (2009).

[62] A. Hedenstrom, L. C. Johansson, M. Wolf, R. Von Busse, Y. Winter, and G. R. Spedding, Bat flight generates complex aerodynamic tracks, Science **316**, 894 (2007).